Newcastle University

ePrints

Patrício SG, Papaioannou EI, Ray BM, Metcalfe IS, Marques FMB.
Composite CO_2 separation membranes: Insights on kinetics and stability.
***Journal of Membrane Science* 2017, 541, 253-261.**

Copyright:

© 2017. This manuscript version is made available under the CC-BY-NC-ND 4.0 license

DOI link to article:

http://dx.doi.org/10.1016/j.memsci.2017.07.008

Date deposited:

11/07/2017

Embargo release date:

08 July 2018

This work is licensed under a
Creative Commons Attribution-NonCommercial-NoDerivatives 4.0 International licence

Newcastle University ePrints - eprint.ncl.ac.uk

Composite CO_2 Separation Membranes: Insights on Kinetics and Stability

S.G. Patrício[a], E.I. Papaioannou[b], B.M. Ray[b], I.S. Metcalfe[b], F.M.B. Marques[a]

[a]Dept. of Materials and Ceramic Eng./CICECO, University of Aveiro

3810-193 Aveiro, Portugal

[b]School of Chemical Eng. and Advanced Materials, Newcastle University

Merz Court, Newcastle upon Tyne NE1 7RU, UK

Abstract

The electrical performance and CO_2 permeation of composite membranes based on Gd-doped ceria skeletons impregnated with molten alkaline carbonates are benchmarked against their predictable performance based on ambipolar conductivity governed kinetics (best scenario), using customized diagrams. Experiments performed in the 550-850 °C temperature range showed permeation rates reaching almost 0.6 $cm^3.min^{-1}.cm^{-2}$ at 850 °C with 50 mol% CO_2 content in the feed side. Endurance tests performed at 650 °C for over 100 h showed a small degradation due to microstructural changes. Impedance spectroscopy measurements combined with microstructural analysis involving several composite membranes and skeletons after distinct thermal history confirmed the potential of these techniques to monitor the ceramic skeleton and membrane condition. The diagrams used to map membrane performance highlight in an entirely novel manner several kinetic and experimental constraints.

Keywords:

CO_2 permeation; impedance spectroscopy; ambipolar conductivity; membrane endurance; composite electrolytes

***Corresponding author:**

fmarques@ua.pt, tel: +351234370269, fax: +351234370204

1. Introduction

Composite electrolytes consisting of a molten alkali carbonate held within a porous oxide support (often a ceria-based electrolyte) have been shown to perform as CO_2 separation membranes with a cooperative transport mechanism involving ions in both molten salt and oxide support. The most common description suggests the counter ionic flow of carbonate and oxide-ions via the two constituent phases [1-10]. In our previous work the performance of these membranes was optimized and the potential of a cooperative mechanism in composites was generalized [11]. The proof of concept for alternative vehicular mechanisms was recently extended to NO_x separation membranes [12]. Considering the underlying purely ionic [1-11] or mixed ionic and electronic mechanisms [12-13], these membranes might be fully or partly selective with respect to a given chemical species. Both situations might be of great practical interest.

These composites rely strongly on the ceramic phase as provider of mechanical stability, besides the role of pathway for oxide-ion transport, since the membranes operate above the carbonates eutectic temperature. To meet this double functionality, the oxide must be a contiguous but porous phase and act as a sponge with respect to the molten carbonates. However, grain boundaries in polycrystalline ceramic electrolytes are known for their blocking characteristics with respect to oxide-ion transport [14]. Thus, the specific interconnection between ceramic grains (e.g., large necks, small necks), an obvious constriction in oxide-ion transport, must be optimized. Furthermore, since at typical working temperatures the ceramic has low conductivity with respect to the carbonates, poor microstructural features will constrain the membrane performance.

While most published results and models consider that membrane performance is governed by coupled ionic transport via oxide and salt, actual results are rarely tested against the predictable performance assuming that ionic transport is indeed rate determining. In this work we map for the first time the performance of our membranes against prediction to comment on likely experimental or kinetic constraints. The outcome of this type of analysis is a deeper understanding of critical aspects often neglected in the analysis of membrane performance.

2. Experimental

The composites studied were based on CGO ($Ce_{0.9}Gd_{0.1}O_{1.95}$, from Praxair, with an average particle size in the order of 120 nm). The CGO powder was firstly coarsened by calcination (1 h) at 1300 °C. The powders were mildly milled with 0.5 wt% PVA (polyvinyl alcohol) before uniaxial pressing (125 MPa) as disks with about 15 mm diameter and 1-2 mm thick. After isostatic pressing (200 MPa), the ceramic skeleton was sintered (at 1300 °C, 4 h) and lastly

impregnated with a eutectic mixture of sodium and lithium carbonates (Sigma-Aldrich, 48:52 molar ratio), hereby named NLC. Impregnation was performed at 700 °C for 90 min, under light vacuum (simple standard laboratory water vacuum pump). The experimental procedure is in all aspects similar to the previously reported [11] except for the (1300 °C) coarsening and sintering temperatures of the CGO powder, which explains the acronym CGO13 adopted to describe these materials. Two sets of samples were prepared in distinct moments from one same powder, named CGO13S1 and CGO13S2. Twin samples from these sets were used to perform complementary microstructural and electrical characterization tests. Sample acronyms, characteristics and tests are listed in Table 1.

Table 1- Characteristics and acronyms of cells tested in this work

Set	Acronym	Processing stage				Testing
		Skeleton	Composite membrane			
		Porosity[a] (%)	Vol.% CGO	Vol.% NLC	Porosity (%)	
1	CGO13S1-1	25	75	19	6	permeation
	CGO13S1-2	21	79	15	6	endurance
	CGO13S1-3	22	78	16	6	impedance, SEM
2	CGO13S2-1	23	77	17	6	permeation, SEM
	CGO13S2-2	23	77	17	6	impedance, SEM

[a]Archimedes method

For the high temperature CO_2 permeation experiments a dual chamber setup was operated at atmospheric pressure (Figure 1). The membranes were mounted on the top of an alumina tube using a sealant (Fuel Cell Materials, silver ink AG-1), separating the feed and permeate side chambers. The sealant was allowed to dry in air before firing under oxidizing conditions at around 550 °C. The active membrane area available for permeation was approximately 0.5 cm^2. The two base gases used, provided by BOC, were a certified mixture of 50 mol% CO_2 + 50 mol% N_2 and pure Ar.

During the permeation experiments the feed-side inlet was composed of a mixture of these gases. N_2 was used to indicate inter-chamber leaks, in order to estimate carbon dioxide leak rates. Ar was used in the permeate side inlet as sweep gas. The flows on both the feed and permeate sides inlets were maintained at 20 cm^3 (STP).min^{-1} for the endurance test and 30 cm^3 (STP).min^{-1} for every other experiment. The outlet permeate-side gases were analysed using

an EES, GeneSys mass spectrometer during the carbon dioxide mole fraction variation test and a HIDEN, HALO 100-RC mass spectrometer for the endurance test. Both were calibrated before the experiments. For permeation experiments the membrane was heated in a temperature programmable furnace up to every operating temperature (from 550 to 850 °C) at 60 °C.h^{-1}. At each temperature the inlet mole fraction of carbon dioxide was varied from 10 mol% up to 50 mol%. The corresponding CO_2/N_2 concentration ratios in the permeate side reached maximum values in the 10-14 range for experiments at 550 °C using 10 mol% CO_2 in the feed gas, and minimum values of 2-3 at 850 °C using 50 mol% CO_2 in the feed gas. Accordingly, the concentration of CO_2 in the permeate side exceeded considerably the estimated leaks in all experiments, although changing with working conditions. One endurance test was performed running the experiment with the higher CO_2 content (50 mol%) for extended periods of time, up to about 100 h, with continuous recording of the permeate-side outlet gas composition.

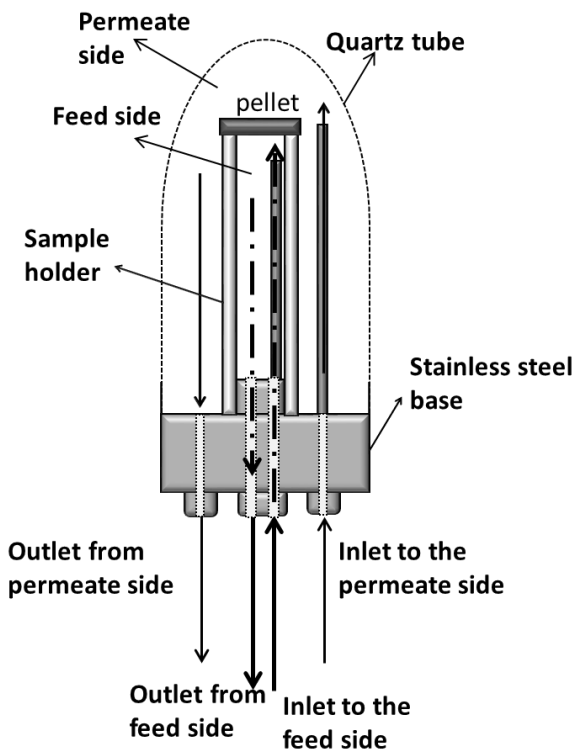

Figure 1 - Scheme of the setup used in the permeation experiments, indicating the relevant gas streams and global assembling.

The CO_2 content in both gas streams ($pCO_{2,feed}$ and $pCO_{2,permeate}$, corresponding to the feed and permeate sides, respectively) is essential for data analysis. The present reactor was described elsewhere [15] and has a good degree of mixing on both the feed and the permeate side. As

first approximation the membrane permeate side was considered as exposed to the outlet condition. Also, $pCO_{2,feed}$ refers to the condition of the feed-side inlet (10 to 50 mol%) considering that the CO_2 mole fraction in the feed side is essentially constant. In fact, at the observed membrane fluxes the mole fraction in the feed side decreases from inlet to outlet by no more than 0.3%.

Ceramic skeletons and composite membranes were studied by impedance spectroscopy (HP 4284A LCR Meter) using a test ac signal amplitude of 0.5 V within the 20 Hz to 1 MHz frequency range (with 10 readings per decade). The measuring conditions were previously validated [16-20]. Prior to the electrical measurements, samples were painted with Au paste and the electrodes fired in air at 600 °C. Gold wires were used as current collectors, with all measurements performed in air within the 200 to 700 °C temperature range.

Microstructural characterization of freshly prepared twin skeletons and membranes was performed by scanning electron microscopy (SEM, Hitachi SU-70) coupled with an energy dispersive X-ray detector (EDS, Bruker Quantax 400). Post-operational analysis of samples used in several experiments also involved impedance spectroscopy and microstructural analysis of the ceramic skeletons after removal of the alkaline carbonates with diluted HCl acid. This set of complementary analyses tried to elucidate the changes observed within the membranes while being tested in permeation experiments.

3. Results

3.1. Microstructural characterization

SEM micrographs of freshly prepared CGO13S1 skeletons and corresponding composite membranes are shown in Figures 2a through 2c. The microstructural characteristics of these membranes are in all aspects similar to those previously reported [11], except for the much smaller average grain size of the CGO grains (light grey), clearly sub micrometric, due to the distinct processing conditions. In Figure 2c we present the combined microstructure and atomic number map distribution (Ce and Na, the easily detected dominant cations of each phase). The presence of interconnected carbonate areas (green/dark grey) between regions where the percolated ceramic phase (red/light grey) prevails shows that the adopted processing route yields dense composite membranes.

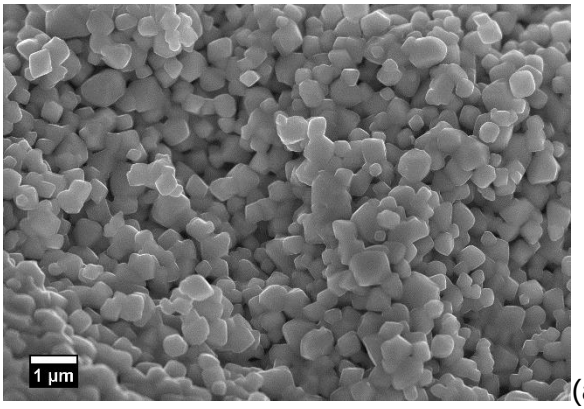

(a)

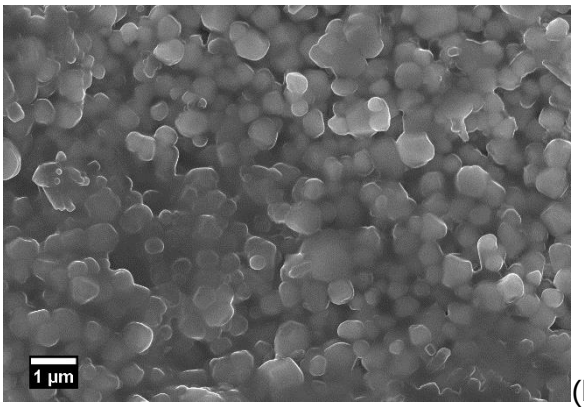

(b)

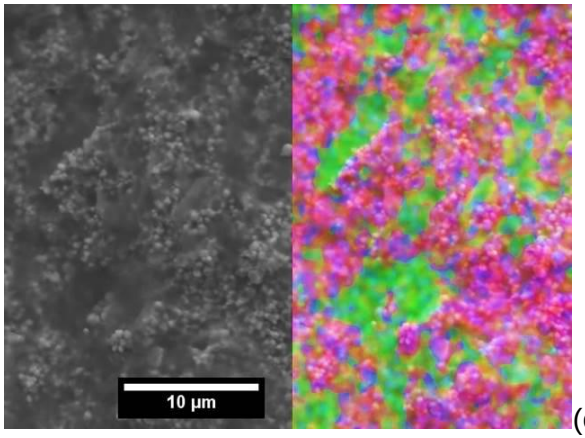

(c)

Figure 2 - Microstructures of CGO13S1 skeletons before (a) and after impregnation (b) at high magnification (10k). For an easier visualization of phase distribution in composite membranes, combined SEM and atomic number maps at 2.5k magnification are also provided in (c). Green (dark grey) and red (light grey) colors correspond to Na and Ce elements, respectively (blue for Gd, in smaller amount).

3.2. Impedance spectroscopy

Figures 3a and 3b include the impedance spectra of the porous CGO13S1 substrates and corresponding composites, in air, at 250 and 600 °C. These two extreme temperatures were selected for providing specific insight on the condition of both phases. Distinct impedance arcs

(at high, intermediate and low frequency) can be discerned based on a systematic study of the roles of ac sign magnitude and dc bias on actual shape of spectra. The low temperature spectra consist mostly of two main contributions related to the materials performance, with linear response. These can be described by two elementary circuits in series, each consisting of a parallel R||CPE arrangement, where R stands for a resistor and CPE for a constant phase element. The analysis of similar impedance spectra was extensively treated in recent publications, and for this reason further details are here omitted [16-20].

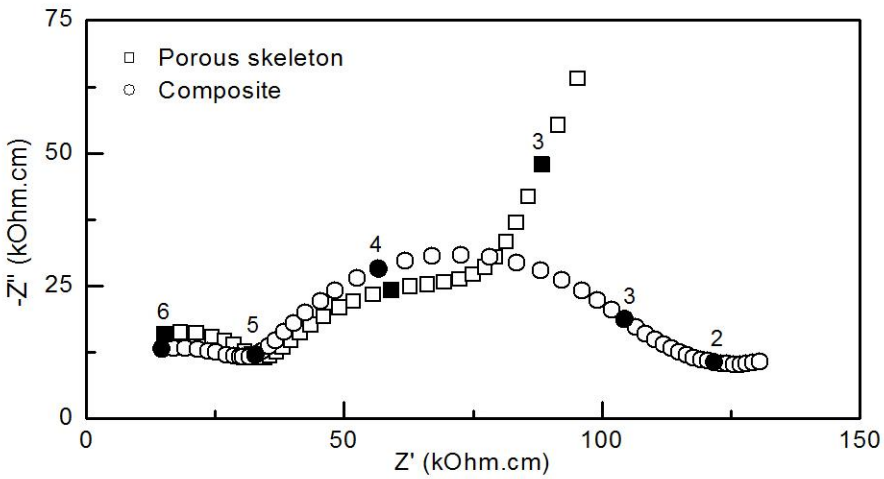

(a)

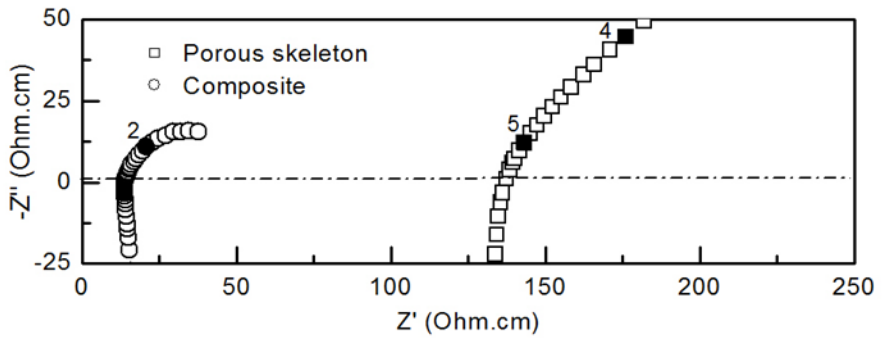

(b)

Figure 3 - Impedance spectra at 250 (a) and 600 °C (b), in air, of CGO13S1-3 (skeleton and composite membrane, microstructures shown in Figure 1a and 1b, respectively). Numbers close to filled symbols indicate the logarithm of the measuring frequency (Hz).

The low temperature (Figure 3a) data confirms the close relation between the electrical properties of the porous skeleton and those of the composite membrane, with the high frequency arc appearing as a fingerprint of a typical ceramic bulk behavior, fully preserved even after impregnation with the carbonates. At intermediate frequency the skeleton impedance is disturbed by the appearance of a large magnitude low frequency arc. Even so, the resemblance between these spectra within the majority of the frequency range clearly confirms that the ceramic phase, the most conductive in this temperature range, determines the electrical

response. The resistive alkaline carbonates act here as a parallel “dormant” pathway, influencing mostly the onset of the lower frequency contribution.

The high temperature spectra of skeleton and composite are distinct in shape but mostly in magnitude (Figure 3b), consisting only of the usually named electrode arc, extending to negative -Z” values due to the setup inductance. Since the composition of both cells is distinct we also have distinct electrode impedances, ignored in the present discussion due to the absence of meaningful data for further analysis.

At high temperature we can measure directly the total conductivity of porous skeletons ($\sigma_{CGO,p}$) and composite impregnated membranes (σ_{comp}) from the high frequency intercept with the Z’ axis. These data provide us an estimate of the actual transport properties of each phase within the membrane, assuming that the composite conductivity is the sum of the parallel contributions of the two phases [18]:

$$\sigma_{comp} = \sigma_{CGO,p} + \sigma_{NLC,p} \quad (1)$$

In equation (1) $\sigma_{i,p}$ (i= CGO or NLC) are the partial conductivities of the two phases within the composite membrane, with the subscript “p” used to distinguish this quantity from the conductivity of the same phase as a fully dense material.

3.3. CO_2 permeation

Figure 4a presents the CO_2 volumetric flux (J_v, $cm^3.min^{-1}.cm^{-2}$) crossing the CGO13S1-1 membrane as a function of temperature, for different CO_2 partial pressures in the feed-side inlet. Permeation increases with the mole fraction of CO_2 in the membrane feed side and also with temperature, but data obtained at higher temperature seems to level off against expectation, as discussed later in this work. The fluxes obtained were also significantly lower than those previously reported for membranes prepared following slightly distinct thermal profiles [11]. All this justified new experiments with a membrane from set CGO13S2. The results obtained with the new set are presented in Figure 4b. The observed trends were closer to expectation, with the permeation flux increasing monotonously with the composition of the feed side and temperature.

The carbon dioxide flux through the CGO13S1-2 membrane over 103 hours at 650 °C, using the higher CO_2 content in the feed-side inlet (50 mol%) is shown in Figure 5 as an endurance test. For CGO13S1-2, irrespective of a short initial decay with fast recovery (probably due to thermal instability during the system start-up), we can notice a slight tendency for declining permeation with time. The final readings are almost 20% lower than the initial reading, after over 4 days of continuous testing. Overall, the magnitude of the observed flux is also in close agreement with the results obtained with the CGO13S2 membrane.

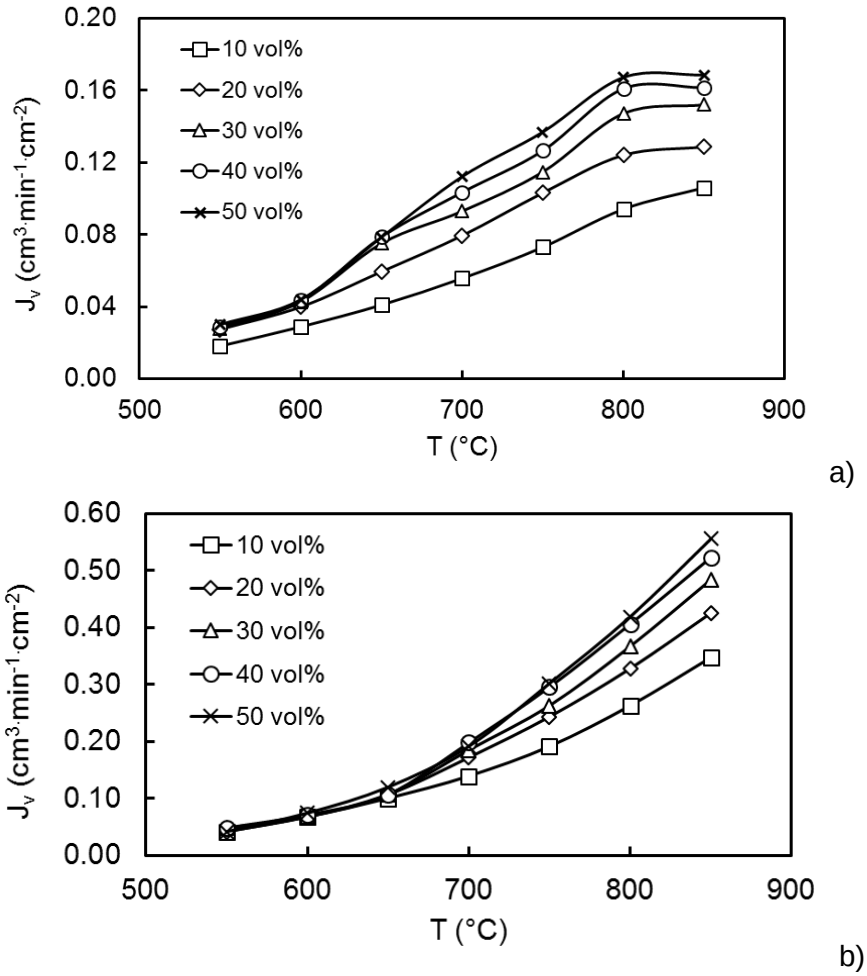

Figure 4 - Carbon dioxide flux (J_v) through the CGO13S1-1 (a) and CGO13S2-1 (b) composite membranes as a function of temperature, for different carbon dioxide contents in the feed-side inlet, as indicated in the inner caption.

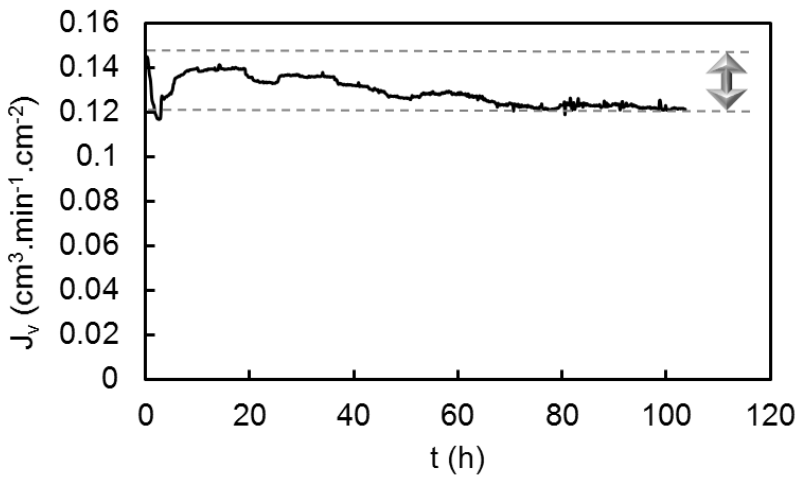

Figure 5 - Carbon dioxide flux through the CGO13S1-2 composite membrane over 103 hours at 650 °C. Feed-side inlet: 50 mol% CO_2 in N_2. Permeate-side inlet: pure Ar.

4. Discussion

4.1. Benchmarking ambipolar conductivity

In composite CO_2 separation membranes a key property is the so-called ambipolar conductivity, σ_{amb} [1-2, 21-22]. Assuming distinct dominant ionic species and transport mechanisms involved in the molten carbonates (e.g., CO_3^{2-}, Na^+, Li^+) and oxide phase (O^{2-}), σ_{amb} can be tentatively described as a function of the partial conductivities of the two phases within the composite [21-22]:

$$\sigma_{amb} = \frac{\sigma_{CGO,p} . \sigma_{NLC,p}}{\sigma_{CGO,p} + \sigma_{NLC,p}} \quad (2)$$

Assuming also that the partial conductivity of each phase in the composite is proportional to the corresponding phase content (simple mixture law), σ_{amb} can be further expressed as a function of the pure phase conductivities (σ_i):

$$\sigma_{amb} = \frac{\varphi . \sigma_{CGO} . (1-\varphi) . \sigma_{NLC}}{\varphi . \sigma_{CGO} + (1-\varphi) . \sigma_{NLC}} \quad (3)$$

where φ is the CGO volume fraction in the composite.

Based on equation (3) and published data on the conductivity of individual phases [23-25] we can draft a model dependence of σ_{amb} on temperature and composition for conditions similar to those used in our experiments. The dependencies predicted for two distinct temperatures (600 and 700 °C) are presented in Figure 6a, where the oxide content changes from 60 to 95 vol%, with 5 vol% increments.

Figure 6a consists of a plot of the ionic transport number of the molten carbonates (t_{NLC}) versus σ_{amb}. By definition an ionic transport number corresponds to the ratio of the conductivity due to one single species to the total conductivity. Grouping again dominant charge carriers in each phase, this yields:

$$t_{NLC} = \frac{\sigma_{NLC,p}}{\sigma_{CGO,p} + \sigma_{NLC,p}} \quad (4)$$

This type of plot was recently introduced [21] to benchmark the electrical performance of these membranes as detailed in the following discussion.

Analysis of equation (3) and Figure 6a shows that σ_{amb} increases with increasing CGO content, the poorly conducting phase, up to peak values around 80-90 vol%, slightly temperature dependent. This is also an upper limit for the oxide content since above this limit the molten carbonates in real microstructures might become trapped and inactive in pools inside the ceramic skeleton. This explains the target porosity values adopted in the present work, close to 20-25 vol%.

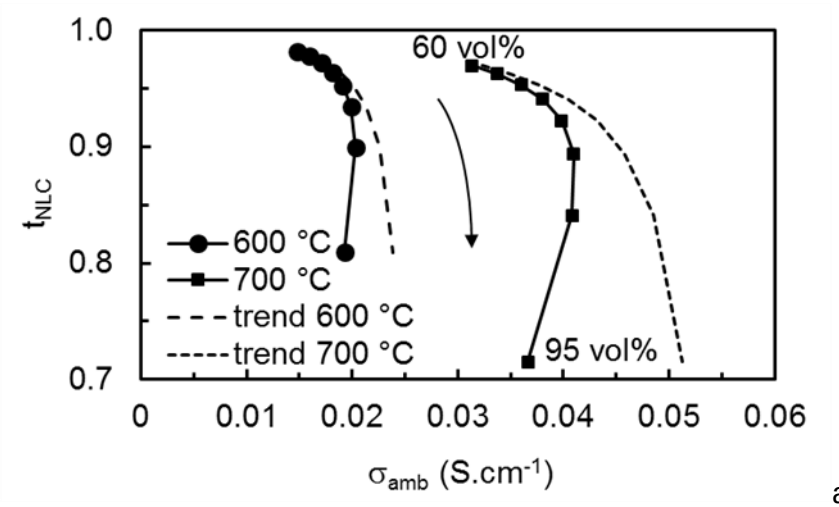

a)

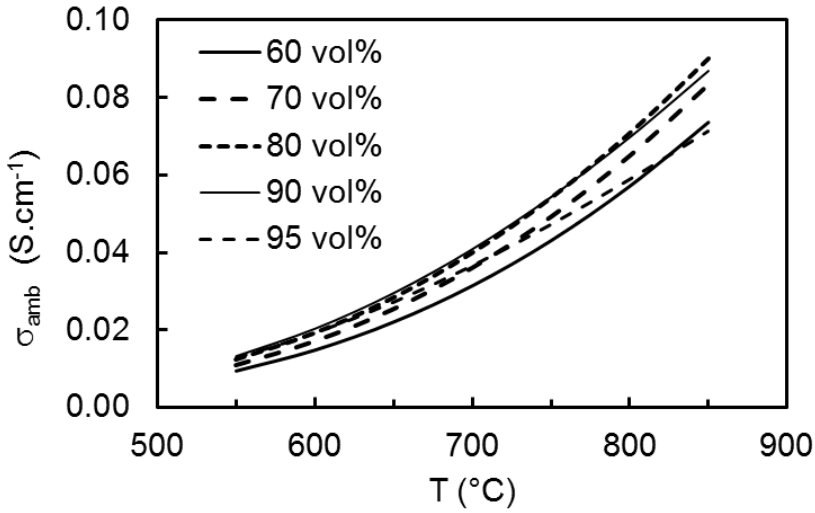

b)

Figure 6 - Model electrical performance of composite membranes: (a) ionic transport number of molten carbonates (t_{NLC}) versus the ambipolar conductivity (σ_{amb}) at 600 and 700 °C, for variable oxide content (60-95 vol% with 5% increments). “Trend lines” correspond to $\varphi.\sigma_{CGO}$, approaching σ_{amb} for oxide contents lower than 80 vol%; (b) σ_{amb} as a function of temperature for distinct oxide contents. See text for further details.

σ_{amb} values approach $\varphi.\sigma_{CGO}$ (named “trend lines” in Figure 6a) for practical compositions where usually $\varphi<0.8$ and $(1-\varphi).\sigma_{NLC} \gg \varphi.\sigma_{CGO}$. This means that potential microstructural constraints in the transport across the ceramic phase should affect strongly σ_{amb}. A severe tortuosity or loss in the percolation of the molten carbonates would be equally influential.

As guidance on model performance, an alternative plot is also presented in Figure 6b, with the temperature dependence of σ_{amb} for each composition. We should have a continuous increase in σ_{amb} with increasing temperature, as a consequence of the temperature dependence of both

partial conductivities. This should be also the tendency for the CO_2 permeation flux through the membrane and explains why results with membrane CGO13S1 were considered abnormal.

As already mentioned, impedance spectroscopy provides all information needed to build plots similar to those presented in Figure 6a. This is shown in Figure 7 using impedance data obtained in the 600-700 °C range, with 50 °C increments. The immediate conclusion from data shown in Figure 7a is that actual membranes perform below ideal performance even considering strictly ionic transport. Actual σ_{amb} values are around 30-40% of the ideal values, but we should recall here that ideal performance neglects all microstructural constraints while actual membranes include features like tortuosity and ion blocking grain boundaries.

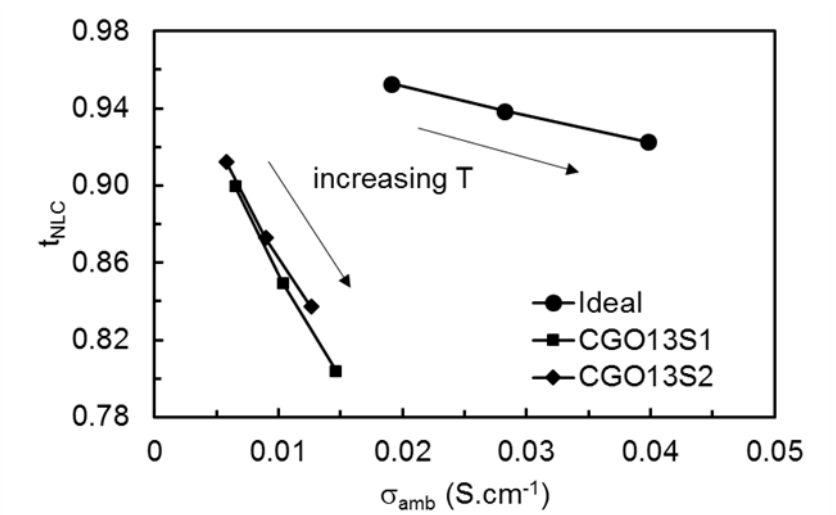

a)

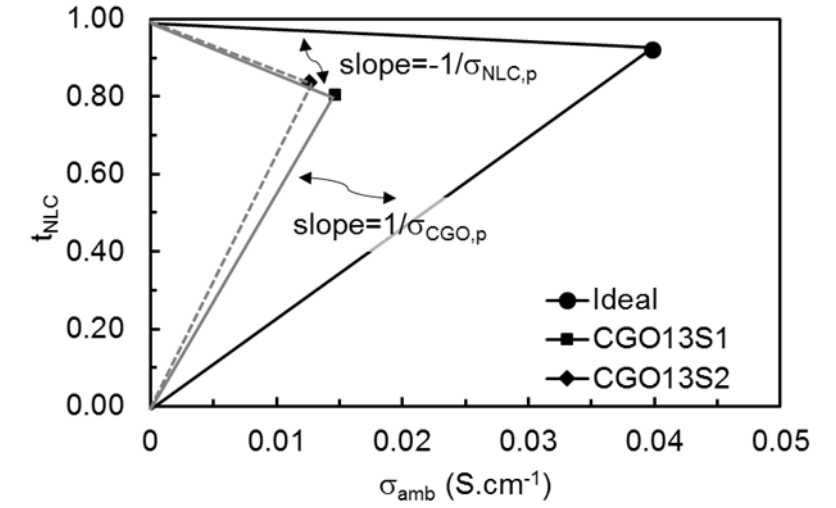

b)

Figure 7 – Plots of t_{NLC} versus σ_{amb} derived from impedance spectroscopy data obtained with composite membranes (also ideal values based on literature data [23-25]): (a) – magnified range covering 600, 650 and 700 °C; (b) – full range plot (only for 700 °C data). Details on information contained in these diagrams can be found in the main text.

The relevance of microstructural features on membrane performance is shown comprehensibly in Figure 7b. The slopes of lines starting at (σ_{amb}, t_{NLC}) points (0, 0) and (0, 1) and ending in distinct (σ_{amb}, t_{NLC}) performance values (real or ideal) are directly related to the partial conductivity of each phase in the composite. From the ratios of these slopes for actual membranes against those corresponding to ideal performance we obtain an estimate for the tortuosity in each phase ($\tau=\sigma_{ideal}/\sigma_{real}$) [2, 9].

The estimated tortuosity values for tested membranes are shown in Table 2. The most impressive result is observed for NLC, with tortuosity estimates in the 6-7 range, increasing slightly with temperature. These values are only expected when isolated pools of carbonates are formed inside the composite [2, 9]. Experimental constraints, namely poor contact between the Au electrodes and the molten phase (during impedance spectroscopy measurements) might explain this apparently overestimated set of values. NLC can be a poorly wetting liquid with respect to usual electrolytes [6] and this might be the source of defective electrical contact with the electrode material, simply bonded to the oxide, the only phase offering a stable high temperature mechanical contact.

Table 2 - Estimated tortuosity in each phase for distinct CGO13 membranes, based on impedance spectroscopy data.

T (°C)	Tortuosity ($\tau=\sigma_{ideal}/\sigma_{real}$)			
	CGO13S1		CGO13S2	
	CGO	NLC	CGO	NLC
600	2.8	6.2	3.2	6.1
650	2.5	6.7	2.9	6.5
700	2.4	6.9	2.9	6.6

With respect to CGO, the tortuosity values (2.4-3.2) are closer to expectation for a porous skeleton [26]. Also, the slight drift to lower tortuosity values with increasing temperature might simply indicate that the role of blocking grain boundaries is vanishing, as expected. We should notice that according to the adopted data handling procedure the role of grain boundaries is grouped with the actual role of phase tortuosity. Overall, these data suggests that the electrical microstructure of these membranes was indeed similar, as expected from data shown in Table 1.

4.2. Benchmarking CO_2 permeation

The current density (J) flowing through a material with conductivity σ and length L, under an applied voltage V, can be expressed as (Ohm's law):

$$J = \frac{1}{L}.\sigma .V \tag{5a}$$

The simplest model used to describe the membrane electrochemical permeation, expressed either as current density (J) or the corresponding CO_2 molar flux per unit area (J_m), obeys a similar relation [1-2, 7]:

$$J = \frac{1}{L}.\xi.\sigma_{amb}.[\frac{RT}{2F}\ \ln\frac{pCO_{2,\ feed}}{pCO_{2,\ permeate}}] \tag{5b}$$

or

$$J_m = \frac{RT}{4F^2L}.\xi.\sigma_{amb}.\ln\frac{pCO_{2,\ feed}}{pCO_{2,\ permeate}} \tag{5c}$$

In equation (5b) the term $\frac{RT}{2F}\ \ln\frac{pCO_{2,\ feed}}{pCO_{2,\ permeate}}$ corresponds to the net thermodynamic voltage (V) experienced by the membrane [22]. σ_{amb} is a function of the pure phase conductivities and volume fractions (equation (3)), while ξ accounts for the global microstructural constraints like pore tortuosity or ceramic inter-grain electrical contact characteristics, effects previously discussed. ξ is a small number when pore tortuosity is high and might be determined from the separate tortuosity values for each phase. L here is the membrane thickness, R is the gas constant, T the absolute temperature and F the Faraday constant. Equation (5c) corresponds solely to the conversion of the ionic current into molar flux (J_m=J/2F).

The above model is based on the assumption of net CO_2 transport fully determined by the membrane ambipolar conductivity. As such, all other steps are neglected. Slow gas/membrane exchange (CO_2 uptake and release) or combination of CO_2 (dissolved in NLC) with O^{2-} (from the CGO matrix), are two examples of possible elementary steps that might hinder the overall transport rate. A new pictorial approach was recently introduced to identify possible kinetic constraints besides ambipolar transport, recalling a treatment widely adopted in the field of corrosion kinetics [22]. Accordingly, the actual CO_2 flux in membranes is mapped in Evans-type diagrams. Such diagrams consist of plots of net thermodynamic voltages (V) versus the effective cell current density (J). Any elementary step can be the source of an overvoltage (ohmic if due to ambipolar transport, non-ohmic if related to surface/interface processes). The sum of all contributions must match the net thermodynamic voltage. These plots include information on ideal and real membrane performance, using a combination of impedance spectroscopy data (to estimate the ohmic contribution), $pCO_{2,feed}$ and $pCO_{2,permeate}$ readings (determining V) and

CO_2 permeation data (converted to current density). A few examples of such plots are shown in Figure 8.

Figure 8a maps the performance of the CGO13S1-1 membrane at two distinct temperatures. The maximum thermodynamic voltage at each temperature is V_{max} and slopes of lines departing from points (0, 0) and (0, V_{max}) are again a simple function of the partial conductivity of each phase. These lines end up when the membrane current density is reached. The ideal current density corresponds to points A (700 °C) and B (600 °C). This result can be obtained using equation (5b) and literature data on the conductivity of each phase [23-25], assuming no microstructural constraints (ξ=1).

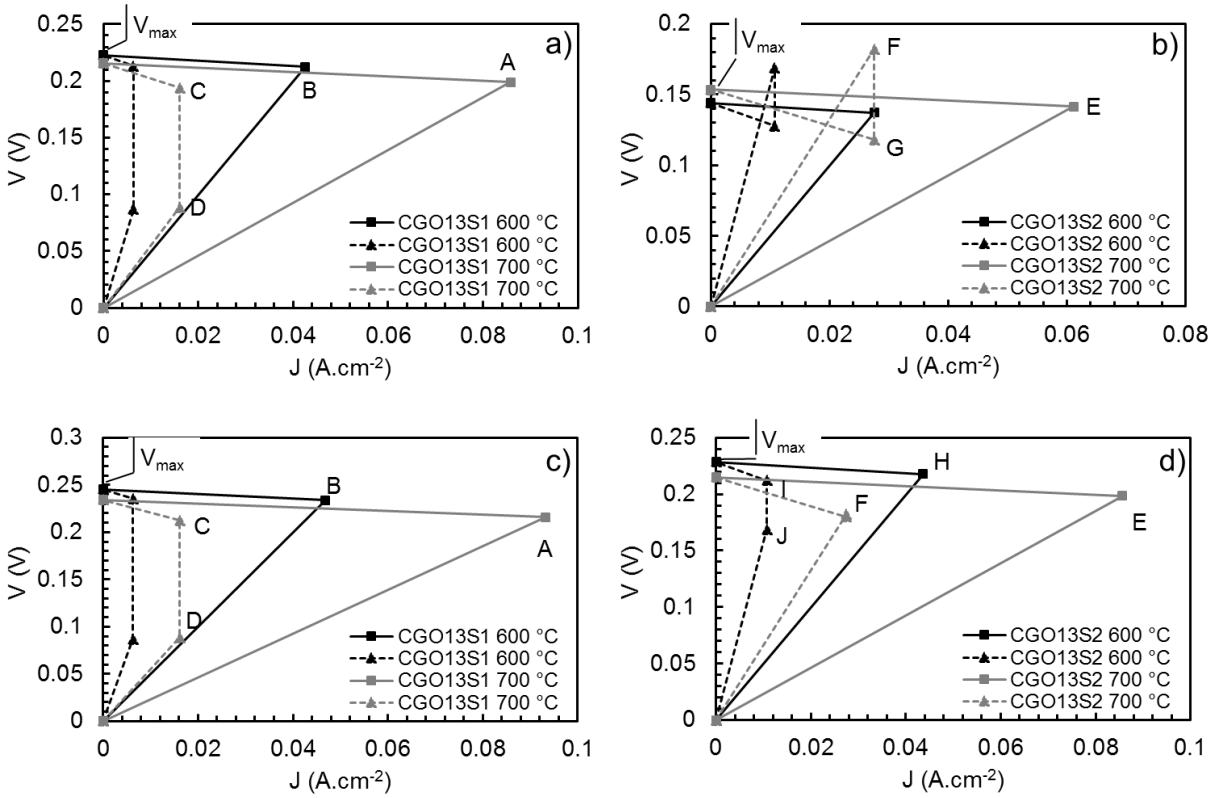

Figure 8 – Evans-type diagrams for the performance of CGO13S1 (a and c) and CGO13S2 (b and d) membranes. In (a) and (b) V_{max} and $pCO_{2,permeate}$ are based on the reactor permeate-side outlet condition (including leaks). In (c) and (d) V_{max} and $pCO_{2,permeate}$ assume simple dilution of the permeation flux in the sweep gas. Points A (a, c), B (a, c), E (b, d) and H (d) correspond to ideal performance (CO_2 flux governed by ambipolar transport). Points or couples CD (a, c), F (d), FG (b), and IJ (d) correspond to real performance. See text for details.

The experimental lines possess distinct slopes due to distinct conductivities. At 700 °C these lines terminate when the actual membrane current density is reached (points C and D). The vertical length of line CD corresponds to an overvoltage related to kinetic constraints other than

ionic transport (e.g., slow surface reaction kinetics). For the CGO13S1-1 membrane the observed current density (permeation) is around 20% of the ideal value and the overvoltage is significant. Similar data obtained at 600 °C is simply shown, without further analysis. As discussed in the following paragraphs, the exact reasons for this low performance might reside in experimental limitations with impact on the cell effective permeating area, rather than global kinetic constraints. However, this set of results was kept as an illustrative example of performance deviating from prediction based exclusively on ambipolar transport.

Figure 8b includes an analogous set of results for membrane CGO13S2, but the picture is totally distinct. The experimental current density apparently exceeds what could be predicted from electrical conductivity measurements. This explains why lines departing from points (0, 0) and (0, V_{max}) cross each other before reaching the experimental current density (points FG, 700 °C). This situation may be due to experimental limitations or to underestimated oxide-ion conductivity, as discussed in the following paragraphs.

The smaller thermodynamic voltage window (V_{max}) in Figure 8b versus Figure 8a suggests experimental constraints since inlet gas mixtures were identical in both experiments. In Figures 8a and 8b the assumed $pCO_{2,permeate}$ readings correspond to the outlet gas concentration, including permeation flux and sealing leaks. The assumption of perfect gas mixing inside the reactor chamber may not be valid. For V_{max} values assuming that $pCO_{2,permeate}$ is only due to the dilution of the CO_2 permeation flux in the sweep gas the modified plots are shown in Figures 8c and 8d. Now the actual performance of membrane CGO13S2 at 700 °C matches closely expectation based on the estimated partial conductivities of both phases (point F in Figure 8d). Thus, an underestimated thermodynamic voltage in Figure 8b seems a possibility. At 600 °C the performance of membrane CGO13S2 (points IJ versus H, Figure 8d) becomes qualitatively similar to the performance of membrane CGO13S1 at 700 °C (points CD versus A in Figures 8a or 8c). Figures 8a and 8c are analogous due to minor sealing leaks in the tests with membrane CGO13S1.

An underestimated conductivity of molten carbonates might also contribute to these results. As previously mentioned, tortuosity values for the molten phase seem unusually high and might be influenced by poor contact between the Au electrodes and the molten phase during impedance measurements. This effect could easily add to the previous one.

Lastly, an enhanced membrane performance with respect to prediction may also reside in limitations in assumed conductivity data, namely a possible contribution of oxide-ions in the molten carbonates. The presence of oxide-ions in molten carbonates due to partial salt decomposition with release of CO_2 is unanimously accepted for many years [27-30]. Even so, there is considerable speculation in the literature on the value of oxide-ion conductivity in molten

carbonates but there seems to be no evidence for a significant magnitude [31-32]. A low oxide-ion conductivity within the molten carbonates would struggle to explain the situation under analysis.

Since membranes CGO13S1 and CGO13S2 were almost twins, the abnormal tendency and low permeation flux at high temperature of membrane CGO13S1-1 suggests a significant degradation mechanism. In order to obtain a deeper insight on likely causes, in Figure 9 we present the measured N_2 content (partial pressure) in the permeate-side outlet. The presence of nitrogen is due to gas diffusion through the molten carbonates and minor sealing problems. These values were used to correct the net CO_2 flux due to electrochemical permeation since both gases were in the feed side in the exact 1:1 proportion. As we can notice comparing Figure 4a and 9, the corrected electrochemical permeation flux tendency is independent of minor fluctuating leaks, changing with the setup temperature. However, the concentration of N_2 is only weakly dependent upon temperature at high temperature, even decreasing between the two highest temperatures. So, in this temperature range both transport of CO_2 and N_2 were inhibited. Migration of the sealing material along the molten phase could explain this blocking effect.

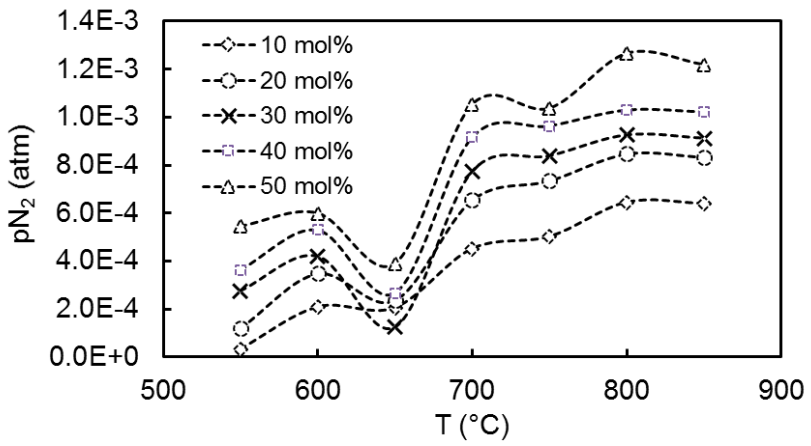

Figure 9 - Partial pressure of nitrogen in the permeate-side outlet. In the inset, values for the N_2 concentration in the feed gas inlet.

Another line of reasoning is also possible, speculating on the membrane stability under specific circumstances. At temperatures above 600-700 °C molten carbonates tend to decompose into CO_2 and alkaline oxides, with the decomposition rate influenced by the exact carbonate mixture and partial pressure of CO_2 [33-34]. This also explains to a large extent that this temperature domain is the upper limit for the operation of Molten Carbonate Fuel Cells where CO_2 is always present in large concentration. In our experiments we should have a faster decomposition of the molten carbonates in the permeate side, since here the CO_2 partial pressure is much lower than in the feed side. Since the conversion to oxide is partial, permeation is not eliminated but

only reduced. An obvious consequence of this type of analysis is that the best permeating membranes should be more stable in the permeate side since with high permeation rates the local concentration of CO_2 at the membrane/sweep gas interface is expected to increase due to mass transfer limitations. Minor CO_2 leaks across the seal would add to this effect. While involving considerable speculation, this aspect should be considered in order to optimize the membrane lifetime and performance.

As already noticed, for the membrane used in endurance tests the initial reading was higher than observed for CGO13S1-1 and closer to CGO13S2-1, but decreased slightly with time. A few *post mortem* tests were performed to try to understand possible reasons for degradation. The membrane was studied by SEM and impedance spectroscopy after removal of the remaining alkaline carbonates to obtain better access to the characteristics of the ceramic backbone. This treatment was also applied to the CGO13S1-1 membrane. Analysis of these membranes by EDS, after attack with HCl and water rinsing, showed no vestige of alkaline carbonates (Na, since Li is not detected) within the detection limits of this technique. The efficacy of chemical etching can be easily understood considering the fast reaction kinetics with visible CO_2 release/bubbling within the acid solution.

Comparison of microstructures of a freshly prepared twin skeleton (Figure 2a), and the backbones of CGO13S1-1 (after permeation tests, Figure 10a) and CGO13-2 (after endurance tests, Figure 10b) after acid attack shows that densification and necks between grains increased for samples exposed to thermal treatment, with the sample used in endurance tests showing the most visible microstructural changes. The result is not surprising considering the previously reported role of alkaline carbonates as sintering aids [35] but also means that working temperatures and/or microstructures must be adjusted to this reality. Interestingly, long term endurance (up to 1000 h) of related composite membranes (same constituents but distinct phase composition and microstructure) at lower operating temperatures (550 °C) provided no sign of degradation if operating in air or carbon dioxide [36]. This suggests an upper limit for the operating temperature for these membranes.

The impact of microstructural changes on the impedance of the ceramic backbone can also be noticed in the impedance spectra shown in Figure 11. Here we compare the skeletons of membranes CGO13S1-1, CGO13S1-2 and CGO13S1-3 after washing with diluted HCl acid. Consistently with previous comments on the analysis of impedance spectra, the high frequency contribution is hardly disturbed by the samples thermal history, emphasizing again the close relation between this arc and bulk CGO performance. The skeleton after endurance (CGO13S1-2) shows the larger interfacial impedance, with the skeleton after impedance (CGO13S1-3) showing the smallest interfacial impedance. This confirms that impedance spectroscopy can be

used to check the condition of these membranes but some limitations should be considered. We are looking at the performance at low temperature (250 °C) and extrapolation to high temperature is only possible assuming that the activation energy for oxide-ion conduction is preserved up to working temperatures (≈ 600 °C), not necessarily true.

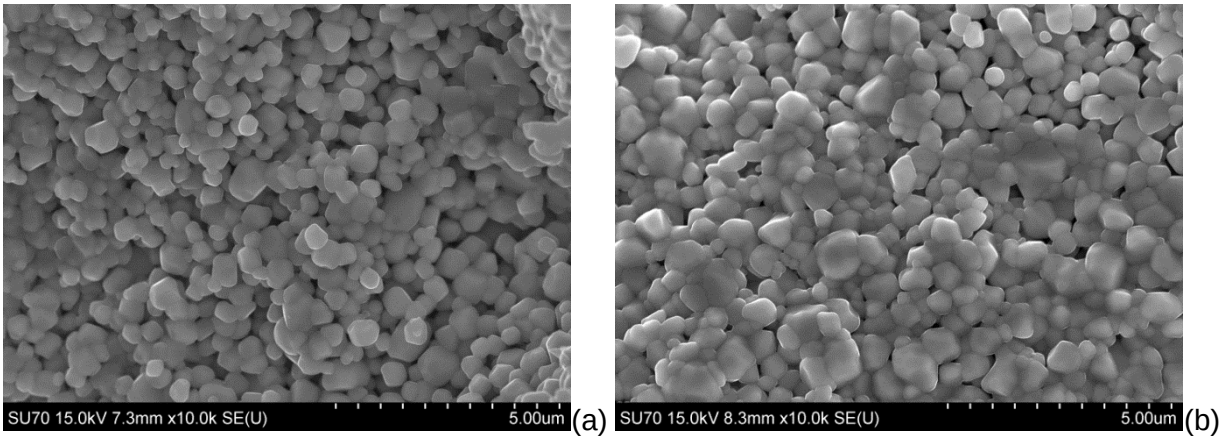

Figure 10 - Microstructures of ceramic porous skeletons: (a) after permeation tests (CGO13S1-1) at variable temperature; (b) after endurance tests (CGO13S1-2). The alkaline carbonates were removed by chemical attack with diluted HCl. Although using distinct markers, pictures have the same 10k magnification as in Figures 2a and 2b.

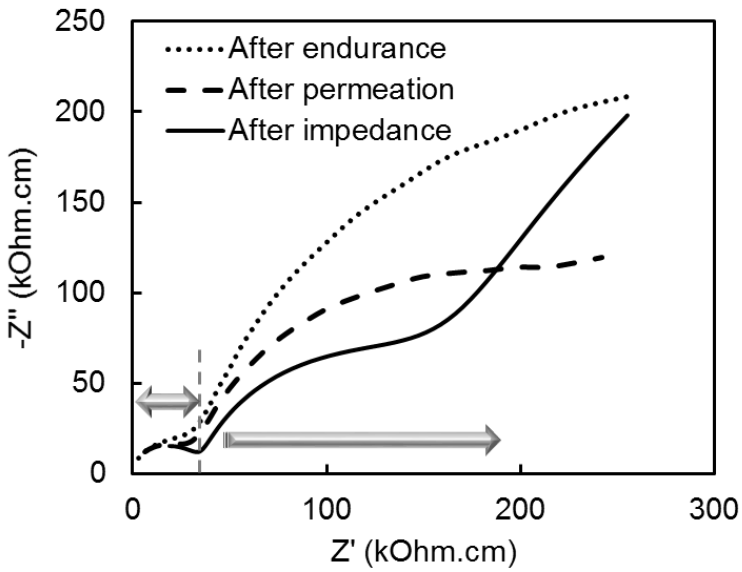

Figure 11 - Impedance spectra at 250 °C in air of similar CGO porous skeletons after impedance (CGO13S1-3), permeation (CGO13S1-1) and endurance (CGO13S1-2). In all cases the alkaline carbonates were removed by chemical attack with diluted HCl. Arrows highlight the high and intermediate frequency ranges.

We also need a physical reason for enhanced interfacial impedance when the material is apparently in a more advanced sintering stage as after prolonged thermal treatments. This seems to be against the common observation of smaller interfacial impedance with the progress of sintering when monitored by impedance spectroscopy [37-38]. The obvious difference is that the low temperature sintering mechanism in this work is assisted by liquid phase diffusion. This means that CGO must dissolve in the molten carbonates to precipitate elsewhere (grain and neck coarsening). But CGO has two distinct cations and the corresponding oxides show a distinct chemical behavior when in contact with molten carbonates. CeO_2 is mostly stable while Gd_2O_3 tends to react [39-41]. This means that the enlarged necks and grains might differ from the base composition, forming a core-shell type microstructure.

Similar situations were observed in the case of yttria stabilized zirconia specimens when exposed to glass melts due to selective loss of yttrium to the melt. The condition was so severe that large cubic zirconia grains even decomposed progressively to smaller monoclinic grains due to the loss of the stabilizing cation [42-43]. So, in the present case we might have a slightly enhanced densification but a shift in the outer grain composition and thus grain to grain interfacial performance. Considering the sub micrometric grain size of CGO, only combined high resolution microscopy and chemical analysis might confirm this hypothesis. While not proven, there seems to be enough ground for speculation on this.

While the present endurance results show some degradation, in recently published data on membrane endurance the reported tendency was the opposite, with a slight enhancement in permeation flux with time for a similar time scale [44]. This was ascribed to a loss in carbonates due to volatilization. A decreasing active membrane thickness increases the overall flux ($J \propto 1/L$). Reported permeation fluxes were in the order of 0.12 to 0.18 $cm^3.min^{-1}.cm^{-2}$ at 650 °C, not far distinct from those now obtained. However, the feed gas mixture had a lower CO_2 content (15 mol%) and significant amounts of oxygen (10 mol%) [44], preventing a direct comparison with our present results. Published microstructural details also prevent a clear comparison between the ceramic skeleton condition before and after tests (although clearly with sub micrometric grain size), but the vol% of the ceramic phase (50%) was lower than in the present work and the relative fraction of molten carbonates was much higher (about twice the hereby adopted). With distinct results obtained with membranes with distinct phase compositions and microstructures there seems to be room for optimization of microstructural features also with respect to long term behavior.

5. Conclusions

The performance of actual composite membranes was benchmarked against prediction based on a standard model where the kinetics is governed by ambipolar conductivity. Experimental results are below expectation although within the usual order of magnitude found in similar experiments. Distinct experimental and performance limitations were duly highlighted using dedicated performance diagrams. Endurance tests performed at 650 °C for about 100 h revealed some degradation in performance. Both SEM and impedance spectroscopy showed effective microstructural changes. Altogether, moderate operating temperatures and tuned microstructures are desirable for enhanced membrane lifetime and performance.

Acknowledgement

The research leading to these results has received funding from the European Research Council under the European Union's Seventh Framework Program (FP/2007-2013) / ERC Grant Agreement Number 320725, from the EPSRC via Grant EP/J016454/1, EP/P007767/1, EP/P009050/1, via Projects NANOMFC (New-INDIGO/0001/2013), CO2ZERO (POCI-01-0145-FEDER-016654 - PTDC/CTM-CER/6732/2014) and CICECO - Aveiro Institute of Materials (Ref. FCT UID/CTM/50011/2013), financed by national funds (Portugal) through the FCT/MEC (PIDDAC) and when appropriate co-financed by FEDER under the COMPETE 2020 Program. S. Patrício thanks FCT for the post-doctoral grant (BPD/75943/2011).

6. References

[1] J.L. Wade, K.S. Lackner, A.C. West, Transport model for a high temperature, mixed conducting CO_2 separation membrane, Solid State Ionics, 178 (2007) 1530-1540.

[2] Z.B. Rui, M. Anderson, Y.S. Lin, Y.D. Li, Modeling and analysis of carbon dioxide permeation through ceramic-carbonate dual-phase membranes, J. Membr. Sci., 345 (2009) 110-118.

[3] Y.D. Li, Z.B. Rui, C. Xia, M. Anderson, Y.S. Lin, Performance of ionic-conducting ceramic/carbonate composite material as solid oxide fuel cell electrolyte and CO_2 permeation membrane, Catal. Today, 148 (2009) 303-309.

[4] M. Anderson, Y.S. Lin, Carbonate-ceramic dual-phase membrane for carbon dioxide separation, J. Membr. Sci., 357 (2010) 122-129.

[5] J.L. Wade, C. Lee, A.C. West, K.S. Lackner, Composite electrolyte membranes for high temperature CO2 separation, J. Membr. Sci., 369 (2011) 20-29.

[6] Z.B. Rui, M. Anderson, Y.D. Li, Y.S. Lin, Ionic conducting ceramic and carbonate dual phase membranes for carbon dioxide separation, J. Membr. Sci., 417 (2012) 174-182.

[7] L.L. Zhang, N.S. Xu, X. Li, S.W. Wang, K. Huang, W.H. Harris, W.K.S. Chiu, High CO_2 permeation flux enabled by highly interconnected three-dimensional ionic channels in selective CO_2 separation membranes, Energ. Environ. Sci., 5 (2012) 8310-8317.

[8] X.L. Dong, J.O. Landeros, Y.S. Lin, An asymmetric tubular ceramic-carbonate dual phase membrane for high temperature CO_2 separation, Chem. Comm., 49 (2013) 9654-9656.

[9] J. Ortiz-Landeros, T. Norton, Y.S. Lin, Effects of support pore structure on carbon dioxide permeation of ceramic-carbonate dual-phase membranes, Chem.l Eng. Sci., 104 (2013) 891-898.

[10] M. Zuo, S.Zuo, X.Y. Tan, B. Meng, N.T. Yang, S.M. Liu, Ionic conducting ceramic–carbonate dual phase hollow fibre membranes for high temperature carbon dioxide separation, J. Membr. Sci., 458 (2014) 58-65.

[11] S.G. Patrício, E. Papaioannou, G. Zhang, I.S. Metcalfe, F.M.B. Marques, High performance composite CO_2 separation membranes, J. Membr. Sci., 471 (2014) 211–218.

[12] G. Zhang, E. I. Papaioannou, I. S. Metcalfe, Selective, high-temperature permeation of nitrogen oxides using a supported molten salt membrane, Energy Environ. Sci., 8 (2015) 1220-1223.

[13] S.J. Chung, J.H. Park, D. Li, J.I. Ida, I. Kumakiri, J.Y.S. Lin, Dual-phase metal-carbonate membrane for high-temperature carbon dioxide separation, Ind. Eng. Chem. Res., 44 (2005) 7999-8006.

[14] X. Guo, W. Sigle, J. Maier, Blocking grain boundaries in yttria-doped and undoped ceria ceramics of high purity, J. Am. Ceram. Soc., 86 (2003) 77–87.

[15] E.I. Papaioannou, H. Qi H, I.S. Metcalfe IS, 'Uphill' permeation of carbon dioxide across a composite molten salt-ceramic membrane, J. Memb. Sci., 485 (2015) 87–93.

[16] A.S.V. Ferreira, T. Saradha, F.L. Figueiredo, F.M.B. Marques, Compositional and microstructural effects in composite electrolytes for fuel cells, Int. J. Energ. Res., 35 (2011) 1090-1099.

[17] C.M.C. Soares, S.G.Patrício, F.M.L. Figueiredo, F.M.B. Marques, Relevance of the ceramic content on dual oxide and carbonate-ion transport in composite membranes, Int. J. Hydrogen Energ., 39 (2014) 5424-5432.

[18] A.I.B. Rondão, S.G. Patrício, F.M.L. Figueiredo, F.M.B. Marques, Impact of ceramic matrix functionality on composite electrolytes performance, Electrochim. Acta, 109 (2013) 701-709.

[19] S.G. Patrício, C.M.C. Soares, C.F.N. Santos, F.M.L. Figueiredo, F.M.B. Marques, Ceria-based substrates for CO_2 separation membranes, Solid State Ionics, 262 (2014) 248–252.

[20] A.I.B. Rondão, S.G. Patrício, F.M.L. Figueiredo, F.M.B. Marques, Role of gas-phase composition on the performance of ceria-based composite electrolytes, Int. J. Hydrogen Energ., 38 (2013) 5497 - 5506.

[21] S.G. Patrício, F.M.B. Marques, Benchmarking the ambipolar conductivity of composite electrolytes for gas separation membranes, Int. J. Energy Res., 40 (2016) 2150–2161.

[22] F.M.B. Marques, S.G. Patrício, E. Muccillo, R. Muccillo, On the Model Performance of Composite CO_2 Separation Membranes, Electroch. Acta, 210 (2016) Pages 87-95.

[23] P.L. Spedding, Electrical Conductance of Molten Alkali Carbonate Binary-Mixtures, J. Electrochem. Soc., 120 (1973) 1049-1052.

[24] B.C.H. Steele, Appraisal of $Ce_{1-y}Gd_yO_{2-y/2}$ electrolytes for IT-SOFC operation at 500 °C, Solid State Ionics 129 (2000) 95-110.

[25] T. Kojima, Y. Miyazaki, K. Nomura, K. Tanimoto, Electrical conductivity of molten Li_2CO_3-X_2CO_3 (X : Na, K, Rb, and Cs) and Na_2CO_3-Z_2CO_3 (Z : K, Rb, and Cs), J. Electrochem. Soc., 154 (2007) F222-F230.

[26] D. Pérez-Coll, E. Sánchez-López, Glenn C. Mather, Influence of porosity on the bulk and grain-boundary electrical properties of Gd-doped ceria, Solid State Ionics, 181 (2010) 1033-1042.

[27] G.J. Janz, Molten carbonate electrolytes as acid-base solvent systems, J. Chem. Educ., 44 (1967) 581-590.

[28] M. Cassir, G. Moutiers, J. Devynck, Stability and Characterization of Oxygen Species in Alkali Molten Carbonate: A Thermodynamic and Electrochemical Approach, J. Electrochem. Soc., 140 (1993) 3114-3123.

[29] S. Scaccia, S. Frangini, Oxygen dissolution behaviour in (52/48) mol% Li_2CO_3/Na_2CO_3 electrolyte containing Ba and Ca additives, J. Mol. Liq. 129 (2006) 133-137.

[30] S. Scaccia, S. Frangini, S. Dellepiane, Enhanced O_2 solubility by RE_2O_3 (RE = La, Gd) additions in molten carbonate electrolytes for MCFC, J. Mol. Liq., 138 (2008) 107-112.

[31] Y. Zhao, C. Xia, Y. Wang, Z. Xu, Y. Li, Quantifying multi-ionic conduction through doped ceria-carbonate composite electrolyte by a current-interruption technique and product analysis, Int. J. Hydrogen Energ., 3 (2012) 8556-8561.

[32] A. Evans, W. Xing, T. Norby, Electromotive Force (emf) Determination of Transport Numbers for Native and Foreign Ions in Molten Alkali Metal Carbonates, J. Electrochem. Soc., 162 (2015) F1135-F1143.

[33] S. Lee, M. Kim, M. Hwang, K. Kim, C. Jeon, J. Song, Thermal stability and viscosity behaviors of hot molten carbonate mixtures, Exp. Thermal Fluid Sci., 49 (2013) 94-104.

[34] R.I. Olivares, C. Chen, S. Wright, The Thermal Stability of Molten Lithium–Sodium–Potassium Carbonate and the Influence of Additives on the Melting Point, J. Sol. Energy Eng., 134 (2012) 041002-1-8.

[35] J.D. Nicholas, L.C. De Jonghe, Prediction and evaluation of sintering aids for cerium gadolinium oxide, Solid State Ionics, 178 (2007) 1187-94.

[36] A.I.B. Rondão, S.G. Patrício, F.M.L. Figueiredo, F.M.B. Marques, Composite electrolytes for fuel cells: Long-term stability under variable atmosphere, Int. J. Hydrogen Energ., 39 (2014) 5460-5469.

[37] D.Z. de Florio, R. Muccillo, Sintering of zirconia–yttria ceramics studied by impedance spectroscopy, Solid State Ionics, 123 (1999) 301–305.

[38] S.K. Tadokoro, T.C. Porfírio, R. Muccillo, E.N.S. Muccillo, Synthesis, sintering and impedance spectroscopy of 8 mol% yttria-doped ceria solid electrolyte, J. Power Sources, 130 (2004) 15–21.

[39] M. Yamauchi, Y. Itagaki, H. Aono and Y. Sadaoka, Reactivity and stability of rare earth oxide – Li_2CO_3 mixtures, J. Eur. Ceram. Soc., 28 (2008) 27–34.

[40] S. Scaccia, S. Frangini and S. Dellepiane, Enhanced O_2 solubility by RE_2O_3 (RE = La, Gd) additions in molten carbonate electrolytes for MCFC, J. Mol. Liq., 138 (2008) 107–112.

[41] F.J.A. Loureiro, S. Rajesh, F.M.L. Figueiredo, F.M.B. Marques, Stability of metal oxides against Li/Na carbonates in composite electrolytes, RSC Adv., 4 (2014) 59943–59952.

[42] C.M.S. Rodrigues, J.A. Labrincha, F.M.B. Marques, Monitoring of the Corrosion of YSZ by Impedance Spectroscopy, J. Eur. Ceram. Soc., 18 (1998) 95-104.

[43] C.M.S. Rodrigues, J.A. Labrincha, F.M.B. Marques, Postmortem characterization of one yttria stabilized zirconia (YSZ)-based oxygen sensor, Solid State Ionics, 136-137 (2000) 671-675.

[44] J. Tong, L. Zhang, M. Han, K. Huang, Electrochemical separation of CO_2 from a simulated flue gas with high-temperature ceramic–carbonate membrane: New observations, J. Memb. Sci., 477 (2015) 1–6.